CANCER

Sequential apoptotic and multiplexed proteomic evaluation of single cancer cells

Emmalyn Lecky[1]†, Atreyi Mukherji[1]†, Rebecca German[1], Gabriella Antonellis[1], Jia-Ren Lin[2], Michael Yorsz[1], Kelley E. McQueeney[1], Jeremy Ryan[1], Kimmie Ng[1], Ewa Sicinska[1], Peter K. Sorger[2], Anthony Letai[1,2]*, Patrick D. Bhola[1,2]*

A potential cause of cancer relapse is pretreatment chemoresistant subpopulations. Identifying targetable features of subpopulations that are poorly primed for therapy-induced cell death may improve cancer therapy. Here, we develop and validate real-time BH3 profiling, a live and functional single-cell measurement of pretreatment apoptotic sensitivity that occurs upstream of apoptotic protease activation. On the same single cells, we perform cyclic immunofluorescence, which enables multiplexed immunofluorescence of more than 30 proteins on the same cell. Using cultured cells and rapid ex vivo cultures of colon cancer patient-derived xenograft (PDX) models, we identify Bak as a univariate correlate of apoptotic priming, find that poorly primed subpopulations can correspond to specific stages of the cell cycle, and, in some PDX models, identify increased expression of Bcl-XL, Mcl-1, or Her2 in subpopulations that are poorly primed for apoptosis. Last, we generate and validate mathematical models of single-cell priming that describe how targetable proteins contribute to apoptotic priming.

INTRODUCTION

A proposed reason for resistance or relapse following chemotherapy is pre-existing populations of tumor cells that are relatively insensitive to cell death. Identifying features of these pre-existing populations may improve biomarkers of therapeutic response or may lead to rational strategies for combination therapies.

Few technologies exist to simultaneously measure the phenotypic properties and high-dimensional molecular features of the same single cell. Performing this for apoptotic phenotypes is particularly challenging because proteases and nucleases that are activated during apoptosis rapidly degrade proteins, transcripts, and genomic DNA and limit subsequent high-dimensional molecular measurements of transcript and protein levels (1, 2). Here, we develop a technique to simultaneously measure apoptotic sensitivity and 30-plex immunofluorescence on acute cultures of cancer cells.

To evaluate apoptotic sensitivity upstream of caspase and nuclease activation, we performed BH3 profiling—a measurement of mitochondrial sensitivity to apoptosis (3). BH3 profiling involves the exposure of mitochondria in plasma membrane–permeabilized cells to synthetic BH3 peptides. For cells that are primed or relatively sensitive for apoptosis, the synthetic BH3 mimetic peptides cause rapid and complete mitochondrial outer membrane permeabilization (MOMP), which is measured at a fixed time point by immunofluorescence of mitochondrial proteins. Cells that are poorly primed bear mitochondria that are relatively insensitive to BH3 peptides. Baseline BH3 profiles correlate with clinical response in many different cancers and represent an important determinant of response to cytotoxic therapy (4, 5). Here, we generate sensitive single-cell measurements of apoptotic priming by performing real-time measurements of single-cell MOMP.

Since many cancer phenotypes are controlled by several proteins acting in concert, it is valuable to simultaneously evaluate the levels of multiple proteins within the same cell. Recent technological advances have been developed to enable multiplexed protein measurements in single cells, including co-detection by imaging, imaging mass cytometry, and cyclic immunofluorescence (CyCIF) (6–8). Here, we use CyCIF which involves staining with three to four fluorescently conjugated antibodies, imaging, chemical bleaching of fluorophores, and repeating over multiple cycles (7). CyCIF has been used to image more than 60 different immunofluorescent antibodies on a single cell (7, 9).

In this study, we leverage BH3 profiling and CyCIF to simultaneously evaluate functional apoptotic signaling and multiplexed protein measurement on individual cells. First, we use live-cell imaging to make sensitive single-cell measurements of apoptotic priming. We subsequently perform multiplexed immunofluorescence using CyCIF, thereby obtaining functional measurements of priming and 30-plex immunofluorescence on the same cell. Using cell lines and 24-hour acute cultures of colon cancer patient-derived xenograft (PDX) models, we identify characteristics of pretreatment populations that are poorly primed for apoptosis. In addition, we generate and validate proteomic mathematical models of apoptotic priming.

RESULTS

Live single-cell method to evaluate priming in cancer cell lines

To perform measurements of single-cell apoptotic priming, we performed live single-cell measurements of MOMP caused by exposure to synthetic BH3 peptides. In contrast to fixed cell measurements of MOMP which typically classify cells as being in a pre-MOMP or post-MOMP state at a single time point (10–12), live cell measurements may identify the time at which cells undergo MOMP, thereby providing a continuous nonbinary classification of apoptotic

[1]Dana Farber Cancer Institute, Boston MA 02215, USA. [2]Harvard Medical School, Boston MA 02215, USA.
*Corresponding author. Email: anthony_letai@dfci.harvard.edu (A.L.); patrick_bhola@dfci.harvard.edu (P.D.B.)
†These authors contributed equally to this work.

priming within a tumor, and better-evaluating diversity in priming within the population.

To measure MOMP using a live-cell readout, we used the cationic dye tetramethyl rhodamine ester (TMRE), which measures a loss of potential across the inner mitochondrial membrane that occurs after MOMP (*13*). Our protocol for live-cell measurements of baseline BH3 profiling is described in Fig. 1. Briefly, cells are plated into 96- or 384-well plates and stained with the mitochondrial membrane potential dye TMRE and the DNA stain Hoechst 33342. Cells are subsequently permeabilized with digitonin, and mitochondria are exposed to synthetic BH3 mimetic peptides. After peptide addition, we perform live-cell imaging to record the time of TMRE loss in each well. We initially tested this assay on HeLa cells and observed that cells retain TMRE in the absence of peptide and release TMRE from mitochondria and the permeabilized cells when synthetic BH3 peptides are added (Fig. 2A and movie S1).

Quantification of apoptotic priming in single cells

To quantify TMRE loss in single cells, we developed an analysis pipeline described in fig. S1. To quantify the peptide-induced loss of TMRE for all single HeLa cells, we first aligned images within wells across different time points based on nuclear Hoechst 33342 staining. Next, using CellProfiler and custom R scripts, the TMRE intensity of individual cells was recorded over time (figs. S2 and S3). Because of different initial concentrations of TMRE in single cells within cell lines, we normalized TMRE intensity to its cumulative maximum value per cell (fig. S3). In plotting TMRE intensity over time for randomly selected cells, we observe a loss of TMRE intensity which indicates MOMP (Fig. 2B). Notably, within a single well, there is cell-to-cell variability of the time of TMRE loss. HeLa cells within a single well that lose TMRE early are relatively primed for apoptosis, whereas cells that release TMRE at later time points are poorly primed for apoptosis (movie S2). To qualitatively evaluate priming across all cells, we plotted the TMRE intensity (color-coded) of individual cells (each cell in a separate *y*-axis row), over time (increasing along the *x* axis) (Fig. 2C).

Next, to quantitatively compare priming across different conditions, for single cancer cells, we calculated the area under the TMRE versus time curve, which integrates the measurement of TMRE intensity across all time points (fig. S4A). We generated a metric of apoptotic priming which is the difference between the area under the curve of a theoretical cell that retains TMRE, and the area under the curve of the cancer cell (fig. S4, B and C). In using this metric to evaluate BH3 profiles of HeLa cells, we observed a dose-dependent increase in apoptotic priming in response to increasing concentrations of the synthetic Bcl-2-like protein 11 (BIM) BH3 peptide (Fig. 2D). In addition, at several synthetic BH3 peptide concentrations, we observed cell-to-cell variability in apoptotic priming (Fig. 2D).

To determine whether the mitochondrial membrane potential at the beginning of the experiment influenced the measurement of apoptotic priming, we compared the initial TMRE intensity in a cell with the TMRE area under the curve metric and found that TMRE loss did not correlate with the initial intensity of TMRE within the cell (fig. S4D). In addition, we found that replicates within the same plate showed similar levels of apoptotic priming (fig. S5). Last, to determine whether there was a positional bias of TMRE loss in the well, we evaluated TMRE loss as a function of the *x* and *y* coordinates of the cell and did not find a visual correlation (fig. S6).

Heterogeneity of apoptotic priming in cancer cell lines

We next sought to evaluate priming heterogeneity in other cancer cell lines by performing real-time BH3 profiling (RT-BP) in the MCF7 and MDA-MB-231 breast cancer cell lines (Fig. 2E and figs. S7 and S8). To evaluate priming, we first used the activator BIM and BH3 Interacting Domain Death Agonist (BID) peptides —which induce MOMP by directly activating the apoptotic effectors Bax and Bak and also inhibit anti-apoptotic proteins (*3*, *14*). We found that the BH3 mimetic activator peptides BIM and BID caused the complete loss of TMRE in all cell lines at high peptide concentrations. Notably at intermediate concentrations of these activator
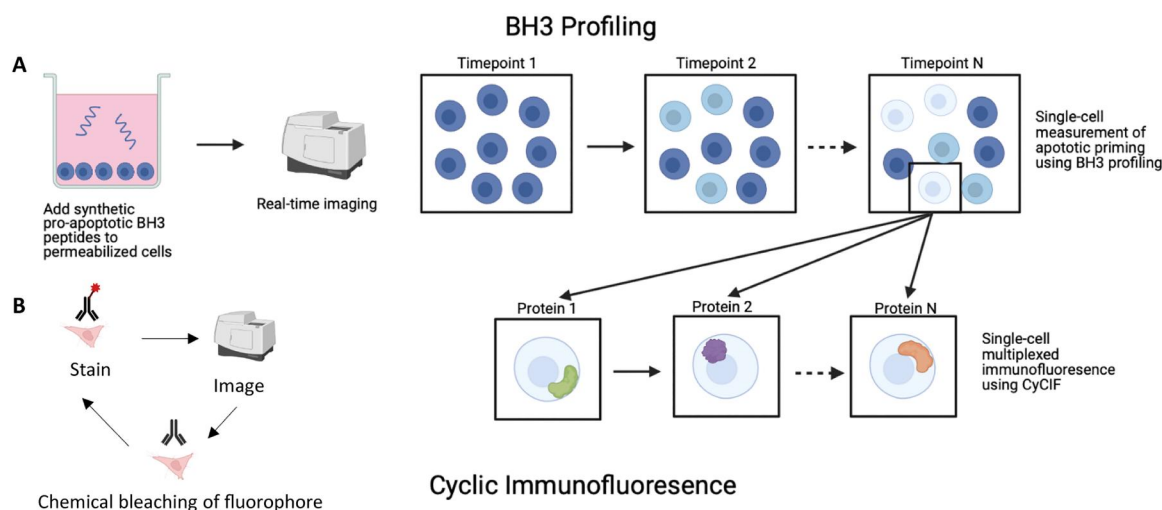
Fig. 1. Schematic of real-time BH3 profiling and cyclic immunofluorescence. (**A**) Live-cell imaging of BH3 peptide–induced TMRE loss is recorded in single cells. Loss of TMRE is depicted as a loss of the blue color in cells over time. Cells that are relatively primed for apoptosis release TMRE faster than the average cell. (**B**) For single cells where BH3 peptide–induced TMRE loss is measured, multiple cycles of antibody staining and immunofluorescence imaging are performed, which enables up to 30 antibody measurements on the single cells from (A).
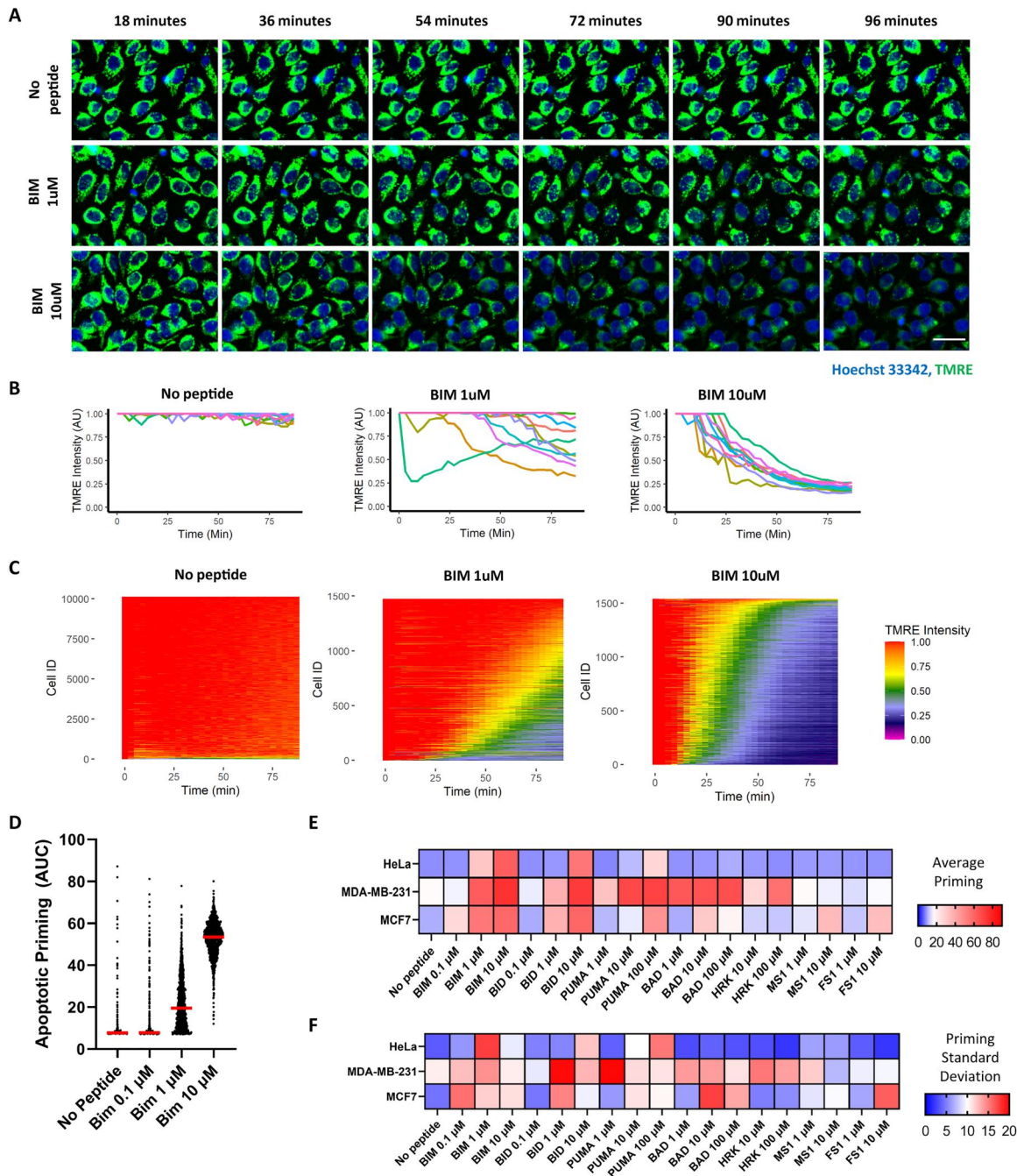
Fig. 2. Real-time BH3 profiling measures single-cell apoptotic priming in HeLa cells. (**A**) Representative time-lapse images of HeLa cells stained with Hoescht 33342 (blue) and TMRE (green) and treated with indicated levels of synthetic BIM BH3 peptides. Scale bar, 50 μM. (**B**) Quantification of TMRE loss in single HeLa cells. Cells treated with indicated concentrations of BH3 peptides. Each line represents 1 of 10 randomly selected cells. AU, arbitrary units. (**C**) Plots of TMRE intensity loss of all HeLa cells during real-time BH3 profiling (RT-BP). Each row is representative of a single cell. Loss of TMRE is represented by the color change from red to purple. (**D**) Violin plots of apoptotic priming for different concentrations of the synthetic BIM peptide; each dot represents a single cell. The mean is represented by red lines. AUC, area under the curve. (**E**) Average apoptotic priming measurements for cancer cell lines. Colors indicate the average apoptotic priming of the population. (**F**) Standard Deviation (SD) of apoptotic priming in cancer cell lines. Red indicates relatively high variability within a well. Data represent a merge of N = 4 biological replicates.

peptides, we could observe cell-to-cell variability in apoptotic priming indicated by a high SD of apoptotic priming (Fig. 2F).

Heterogeneity of priming in artificially mixed cancer cell lines

We next sought to evaluate whether we could artificially mix cell lines with different levels of apoptotic priming and correctly identify single cells using RT-BP. To evaluate this, we used HeLa cells in which the apoptotic effector proteins Bax and Bak are knocked out [HeLa DKO (double knockout)], and which hence do not undergo MOMP in response to pro-apoptotic stimuli. We first mixed varying populations of HeLa wild-type (WT) and HeLa DKO cell lines, performed real-time BH3 profiling (RTBP), and found that only a fraction of the cells underwent TMRE loss (Fig. 3, A and B, and movie S3). In addition, when we calculated the mean apoptotic priming for specific cell ratios, we found a correlation between apoptotic priming and the fraction of DKO cells that were plated (Fig. 3C).

To evaluate the sensitivity and specificity of RT-BP to detect single poorly primed cells, we used equal mixtures of the HeLa WT and HeLa DKO cells, performed BH3 profiles, and compared single-cell measurements of apoptotic priming with subsequent Bak immunofluorescence on the same cell. We expected that cells that lack Bak would be poorly primed for apoptosis relative to WT cells (15). We observed that cells with high levels of Bak were more primed for apoptosis relative to cells with low levels of Bak ($P < 0.0001$) (Fig. 3D). In addition, using the gold standard that cells that are positive for Bak should be primed for apoptosis, and cells that are negative for Bak should be poorly primed for apoptosis, we performed a receiver operator characteristic analysis to determine how well apoptotic priming predicted Bak expression in the mixed samples (Fig. 3E). We observed a receiver operating characteristic area under the curve measurements of 0.989 indicating that, in these mixed experiments, RTBP was a sensitive and specific predictor of poorly primed cells in artificially mixed populations.

Cyclic immunofluorescence on single cancer cells after BH3 profiling

We next asked if we could identify the molecular features of cells that are highly or poorly primed for apoptosis. Therefore, after performing RT-BP, we performed CyCIF—a multiplexed imaging strategy resulting from multiple cycles of staining, imaging, and fluorophore bleaching (7). We first sought to determine whether BH3 profiling was compatible with CyCIF. Since BH3 profiling permeabilizes the plasma membrane, we expect that several proteins may leave the cell. To evaluate this loss, we compared protein immunofluorescence before and after BH3 profiles (fig. S9A). We found that the fluorescence intensity of proteins that were in or attached to organelles was retained, while proteins that were unanchored [such as high mobility group box 1 protein (HMGB1)] were lost (fig. S9, A to C). Last, to determine whether decreased cell attachment due to BH3 profiling was compatible with multiple cycles of CyCIF, we performed several cycles of CyCIF and evaluated the cell loss, finding that, in cell lines, we could keep up to 91% of cells after seven cycles of bleaching, staining, imaging (fig. S9, D and E). Notably, there was no difference in apoptotic priming between cells that were retained over seven cycles and cells that were lost (fig. S9F).

Univariate correlation of apoptotic priming with immunofluorescence in single cells

We next sought to determine whether there were protein measurements correlates of apoptotic priming in cancer cell lines. We first performed RT-BP with the synthetic BIM peptide on HeLa cells (Fig. 4A) and subsequently performed seven cycles of CyCIF using a panel of antibodies (Fig. 4B and fig. S10). This panel of antibodies included Bcl-2 family proteins, markers of the cell cycle, markers of EMT transition, and DNA damage (Fig. 4C and table S1).

To correlate apoptotic priming with multiplexed immunofluorescence, we linked measurements of apoptotic priming with protein intensities over seven cycles of CyCIF based on the geographic coordinates of cells. Specifically, all images were registered to align with the last time point of the real-time BH3 profile images, and intensities were measured using CellProfiler and custom R-scripts (fig. S1). We next ranked individual cells according to measured apoptotic priming and represented protein levels in each cell as a heatmap (Fig. 4C). For HeLa cells treated with 10 μM of the BIM peptide, we observe a correlation between apoptotic priming and Bak protein expression (Pearson's $r = 0.29$, $P = 0.002$; Fig. 4, C and D, and movie S4).

Next, to evaluate patterns of molecular correlates of priming, we performed RT-BP and CyCIF in MCF7 and MDA-MB-231 cells. For a single-cell line, we evaluated univariate Pearson's correlation coefficients between single-cell apoptotic priming and immunofluorescence staining (Fig. 4E). We found that the Bak protein expression correlated with priming was induced by the synthetic BIM peptide for all three cell lines. Within a single-cell line for specific synthetic BH3 peptides, we could find single-cell correlates of priming. For instance in MCF7 cells, we observed a correlation between apoptotic priming and proliferating cell nuclear antigen (PCNA), a marker of DNA replication (Fig. 4E). These data suggest that for some, though not all, cells we could identify univariate protein correlates of BH3 profiling.

Correlation of multiple immunofluorescence markers with priming

Leveraging functional single-cell measurements of priming and 30-plex imaging of single cells, we next asked if there were subpopulations that corresponded to relatively high or low levels of apoptotic priming based on expression patterns of many proteins. To do this, we first performed t-distributed stochastic neighbor embedding (tSNE) to cluster HeLa cancer cells based on protein levels, and then color-coded cells on the tSNE plot according to the measured priming values (Fig. 5A and fig. S11). In HeLa cells exposed to 10 μM of the synthetic BID peptide, we identified a subpopulation (labeled as SP1) that shows relatively poor apoptotic priming (Fig. 5, A and B). Using tSNE coordinates, we calculated the mean difference of individual protein or dye stain levels between the SP1 subpopulation and all other cells (Fig. 5C). We determined that the poorly primed subpopulation is characterized by a high amount of genomic DNA (as indicated by the high Hoechst 33342 staining) and low levels of PCNA— a protein that is expressed during DNA replication (16). This high-Hoechst and low-PCNA state can also be identified in tSNE plots where protein levels are represented by a color (Fig. 5D) and by scatter plots of Hoechst intensity and PCNA immunofluorescence (Fig. 5E and movie S5).
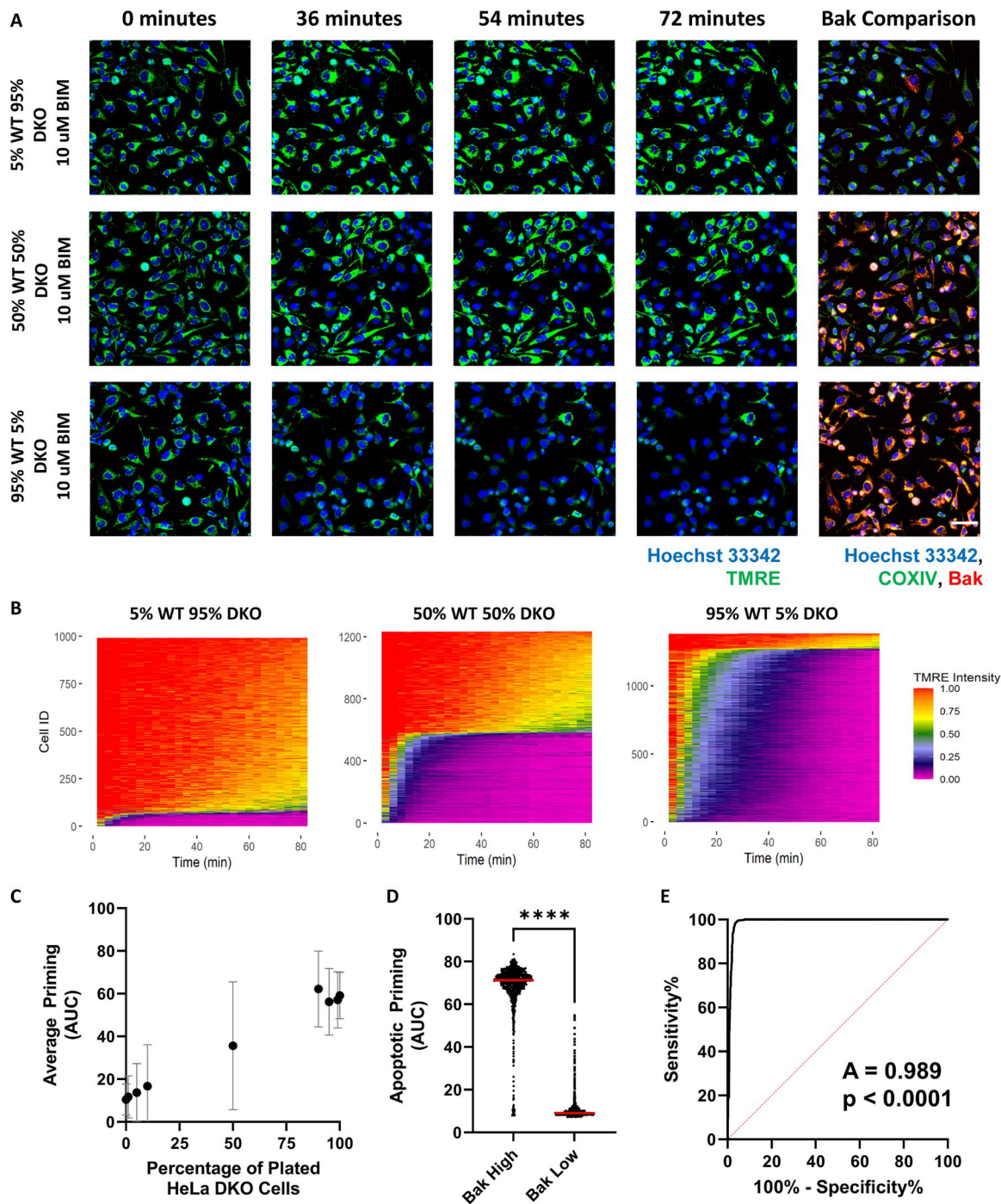
Fig. 3. Real-time BH3 profiling of artificially mixed cultures of primed and poorly primed cancer cells. (**A**) Representative RT-BP images of HeLa wild-type (WT) and Bax/Bak double knockout (DKO) cells stained with Hoescht 3342 (blue) and TMRE (green). Cells were also stained for Bak (red) and Cytochrome c oxidase subunit 4 (COXIV) (green) on the same single cells after the RT-BP. Scale bar, 50 μM. (**B**) Plot of TMRE intensity versus time for all HeLa cells. Each row is representative of a single cell. Loss of TMRE is represented by the change from red to purple. (**C**) Plot of the percent of HeLa WT cells in each well against the average priming of all cells in each well. Error bars represent the SD of all cells. (**D**) Plot of single-cell apoptotic from the tsunami plots for a mix of 50% HeLa WT and 50% HeLa DKO cells with high Bak intensity versus low Bak intensity. Each dot represents a single cell. ****$P < 0.0001$ using t test. (**E**) Receiver operator characteristic describing whether apoptotic priming measured by RT-BP predicts Bak immunofluorescence for an equal mix of HeLa WT and HeLa DKO cells ($A = 0.989$, $P < 0.0001$). Data represent a merge of $N = 4$ biological replicates.
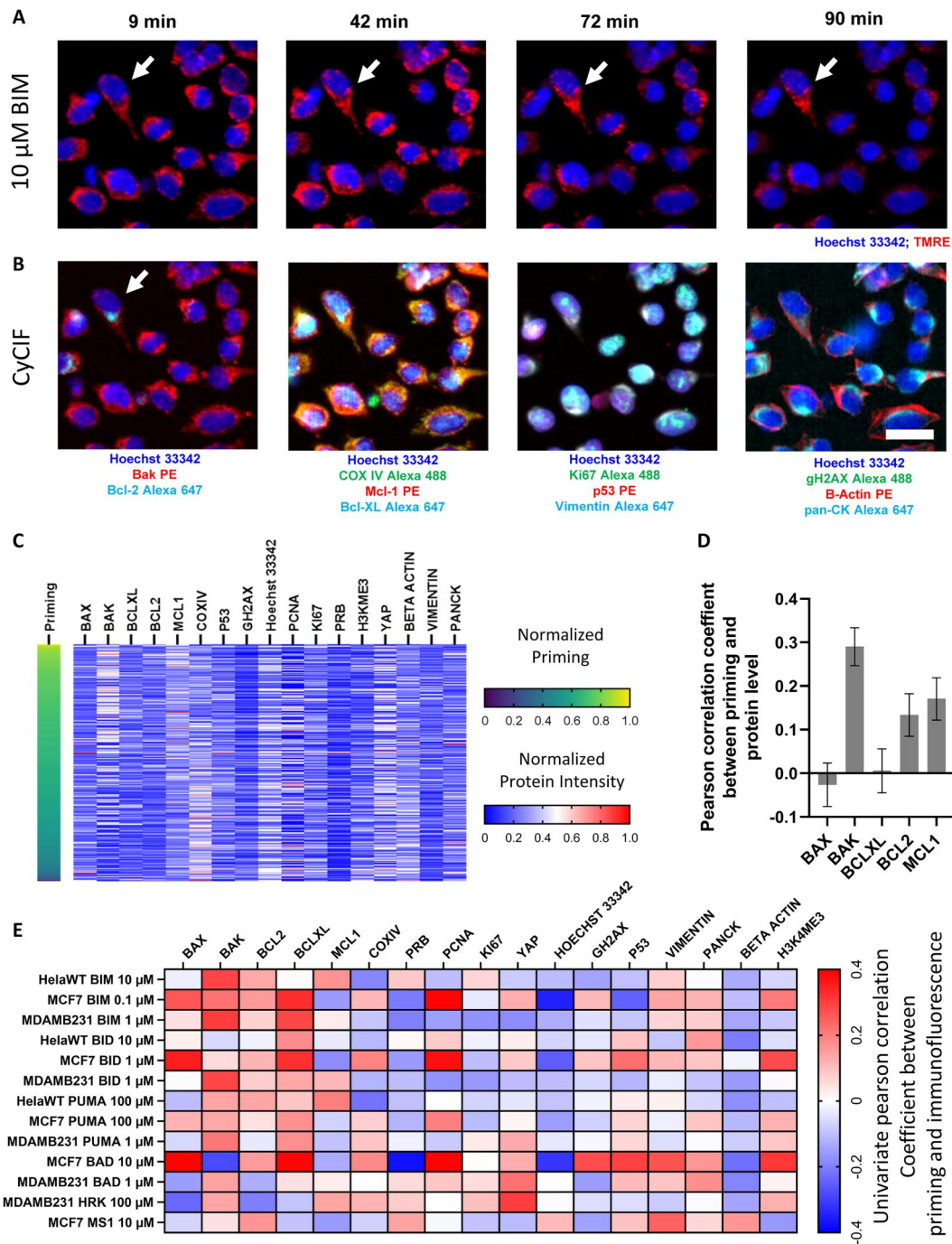
Fig. 4. Multiplexed immunofluorescence after BH3 profiling indicates that Bak expression correlates with priming in HeLa cells. (**A**) Representative images from RT-BP with 10 μM BIM. The indicated cell (arrow) is poorly primed and retains TMRE throughout the 90-min time course. Scale bar, 50 μm. (**B**) Representative images from CyCIF cycles corresponding to the cells in (A). (**C**) Heatmap displaying apoptotic priming and protein immunofluorescence in HeLa cells treated with 10 μM BIM. Each row represents a single cell. Cells are arranged from most primed (top row, yellow) to least primed (bottom row, purple). Each column represents a protein immunofluorescence measured during CyCIF. Protein levels range from red (highly expressed) to blue (poorly expressed). (**D**) Pearson's correlation coefficient of Bcl-2 family protein expression and apoptotic priming in HeLa cells treated with 10 μM BIM. Error bars represent a 95% confidence interval of the correlation coefficient. (**E**) Heatmap displaying Pearson's correlation coefficients between protein immunofluorescence and apoptotic priming across different cell lines and peptides. Red indicates a high correlation with priming; blue indicates a poor correlation with priming. Data represent a merge of $N = 2$ biological replicates.
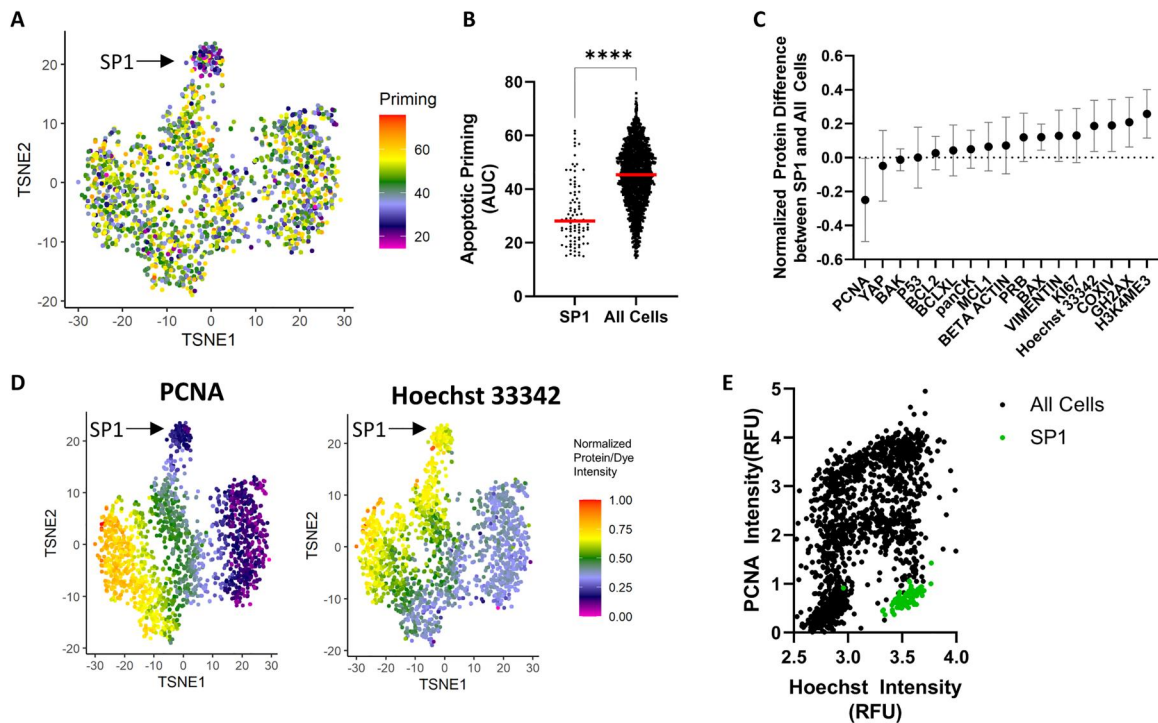
Fig. 5. The correlation of multiplexed immunofluorescence with apoptotic priming indicates cell cycle states that are poorly primed for apoptosis. (**A**) tSNE plot of HeLa cells exposed to 10 μM of the synthetic BID peptide and their respective apoptotic priming values. Higher apoptotic priming is indicated in red, while lower apoptotic priming is indicated in purple. SP1 indicates a subpopulation of poorly primed cells. (**B**) Comparison of apoptotic priming in the SP1 population from (A) and the rest of the population. The mean is indicated by red lines. ****$P < 0.0001$ using t test. (**C**) Plot of the normalized protein or dye difference between HeLa subpopulation SP1 and all HeLa cells. A high difference indicates a protein/dye preferentially expressed in SP1, and a negative difference indicates a protein/dye preferentially decreased in SP1. Error bars represent the SD of protein/dye intensity for all cells. (**D**) tSNE plot of all HeLa cells exposed to 10 μM of BID and their PCNA protein intensity or Hoechst 33342 stain intensity. High protein/dye intensity is indicated by red, and low protein intensity is indicated by pink. (**E**) Identification of SP1 subpopulation on a PCNA-Hoechst 33342 scatter plot. Data represent a merge of $N = 2$ biological replicates.

Similar results were observed in HeLa cells exposed to the synthetic BIM peptide (fig. S12).

We reasoned that this population of poorly primed corresponds to a subpopulation that follows the S phase in the cell cycle but precedes cell division. Notably, there is a poor single-parameter correlation between Hoechst 33342 staining or PCNA immunofluorescence and apoptotic priming (Fig. 4E), highlighting the value of multiparametric measurements of single cells. For MCF7 cells, we identified a poorly primed subpopulation that corresponded to the G1 phase of the cell cycle (fig. S13, A to C). However, there was no obvious poorly primed subpopulation for MDA-MB-231 cells (fig. S13D).

Univariate and multivariate relationships between apoptotic priming and immunofluorescence in colon PDX models

Prolonged ex vivo cultures of human or mouse tumors may change the chemical vulnerabilities of cancer cells (10). Therefore, in addition to cultured cell lines, we sought to perform functional measurements of apoptotic priming and 30-plex molecular measurements for rapid 24-hour ex vivo cultures of cells from six colon PDX models. Colon PDX models had been transplanted directly from humans into mice and were not cultured ex vivo before these experiments.

First, to evaluate the heterogeneity of apoptotic priming in the colon PDX models, we performed real-time BH3 profiles using the synthetic BIM BH3 peptide for six colon PDX models, followed by CyCIF on the same cells. These proteins included the Bcl-2 family, markers of the EMT transition, cell cycle markers, markers of DNA damage, and stress response. A representative example of the COCA235 PDX model is shown in Fig. 6 (A to D). We observed a loss of TMRE intensity over time for COCA235 cells treated with 1 μM of the synthetic BIM BH3 peptide (Fig. 6A). In performing CyCIF on the same cells, we could evaluate both apoptotic priming and protein immunofluorescence for all single cells (Fig. 6, B and C).

We first sought to evaluate univariate Bcl-2 family protein correlates of apoptotic priming for the COCA235 PDX model and observed an inverse correlation between apoptotic priming and expression of the anti-apoptotic protein Mcl-1 (Fig. 6, C and D). We also quantified univariate Pearson's correlation coefficients between priming and immunofluorescence for all individual proteins in six PDX models (Fig. 6E and fig. S14). Note that, for four of the six PDX models, there is a positive correlation between priming and the pro-apoptotic Bak protein (Fig. 6E).

To qualitatively identify multivariate features of poorly primed subpopulations, we first generated tSNE plots for each colon PDX model based on protein immunofluorescence and overlaid quantifications of single-cell apoptotic priming (Fig. 7A and fig. S15). For
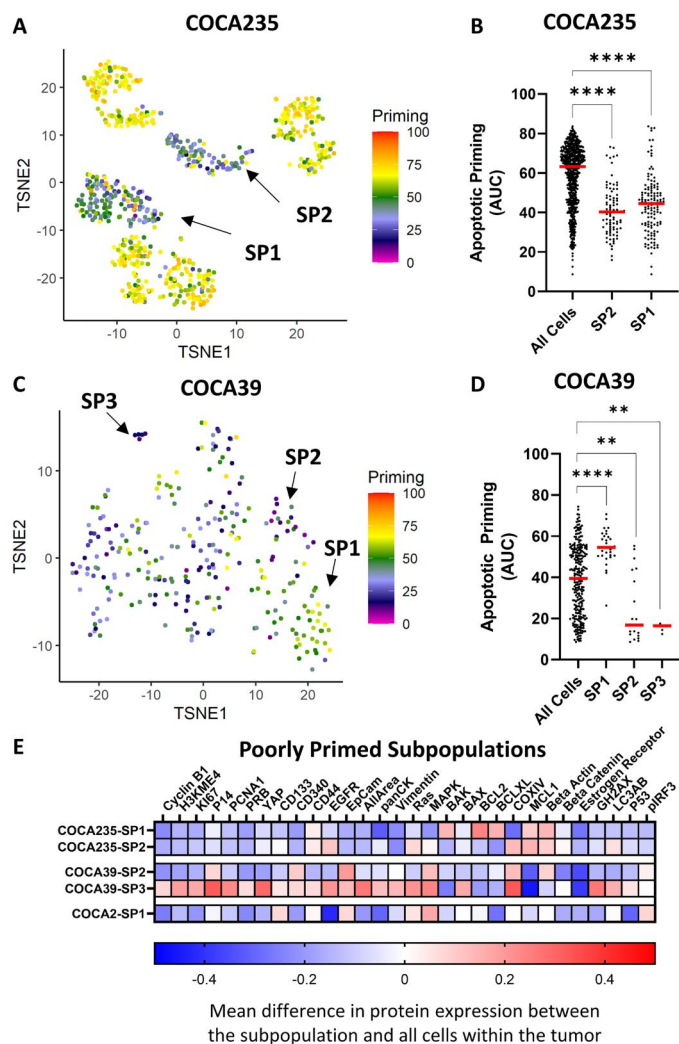
Fig. 6. Apoptotic priming and cyclic immunofluorescence on 24-hour cultures of colon cancer PDX cells. (**A**) Representative images from RT-BP on COCA235 treated with 1 μM BIM. (**B**) Representative images of various protein markers acquired from CyCIF in COCA235. Scale bar, 50 μm. (**C**) Heatmap displaying priming and protein expression in COCA235 cells treated with 1 μM BIM. Each row represents a single cell. Cells are arranged from most primed (top row, yellow) to least primed (bottom row, purple). Protein expression levels are indicated from red (highly expressed) to blue (poorly expressed). (**D**) Graph displaying Pearson's correlation coefficient between protein expression and apoptotic priming in COCA61 cells treated with 1 μM BIM. Error bars represent a 95% confidence interval of Pearson's correlation coefficients. (**E**) Heatmap displaying Pearson's correlation coefficients between protein levels and priming across different colon PDX tumors. Data represent a merge of $N = 2$ biological replicates.

the COCA235 PDX model, we identified two subpopulations that were less primed for apoptosis relative to the average of all cells (Fig. 7, A and B). Conversely, for COCA39, we identified two poorly primed subpopulations of cells and a relatively highly primed subpopulation of cells (Fig. 7, C and D). Notably, for some of the colon PDX models, we could not identify a

subpopulation that was associated with high or low apoptotic priming (fig. S15).

To identify features of highly or poorly primed subpopulations, we quantified the mean protein levels of the highly primed or poorly primed subpopulations relative to mean protein levels across the entire population. For COCA235, both poorly primed

Fig. 7. Subpopulations of colon PDX tumors that are highly or poorly primed for apoptosis. (**A**) tSNE plot of COCA235 cells based on protein expression. Each dot represents a single cell. Colors indicate relative apoptotic priming values. Higher apoptotic priming is indicated in red; lower apoptotic priming is indicated in pink. (**B**) Apoptotic priming of subpopulations of COCA235 in (A). (**C**) tSNE plot of COCA39 cells based on protein expression. Each dot represents a single cell. Colors indicate relative apoptotic priming values. (**D**) Apoptotic priming of subpopulations of COCA235 in (C). (**E**) Mean difference between protein expression within a poorly primed subpopulation and average protein expression. t tests were performed in (B) and (D) to evaluate differences between all cells and the subpopulations. **$P < 0.001$ and ****$P < 0.0001$.

subpopulations were characterized by relatively high levels of the anti-apoptotic protein Mcl-1 and low levels of vimentin (Fig. 7E). For COCA39, two poorly primed subpopulations expressed high levels of Her2 (CD340) relative to the average Her2 expression of the entire population (Fig. 7E).

Mathematical models of apoptotic priming based on protein immunofluorescence

To determine how different proteins might contribute to priming as a part of a whole system, we sought to generate linear mathematical models of apoptotic priming using linear regression and evaluate

how each protein contributes to the model. For tumors with sufficient cell numbers, we split the single-cell dataset in half and used half of the dataset to train the linear models, and the other half to validate the linear models (Fig. 8, A and B, and fig. S15). For COCA235, there was a linear correspondence between expected priming based on the protein level, and the measured apoptotic priming (Fig. 8B). To evaluate the fit of each model, we evaluated Pearson's correlation coefficients between predicted and actual priming using the validation dataset (Fig. 8C). Note that, for COCA8, there is a poor fit between actual and predicted priming (Fig. 8C and fig. S16).

To understand the relative contributions of individual proteins to the model, we evaluated the coefficients of linear regression models (Fig. 8D). For some tumors where a protein is a poor univariate correlate of priming, we find that the protein is important to the linear mathematical model. For example, in COCA61 and COCA235, Bak is a poor univariate correlate of apoptotic priming (Fig. 6E) but is an important parameter for the linear model (Fig. 8D). This suggests that Bak may be an important modulator of priming for COCA61 and COCA235, but only in the relative context of other proteins.

Because of the potential nonlinear relationships between protein levels and priming, we next asked if a nonlinear mathematical model was a superior predictor of priming. We split the dataset for each tumor (70% for training, 30% for validation) and used random forest regression to train and test mathematical models of apoptotic priming based on protein levels for each specific tumor. We observed a correspondence between actual and predicted priming for both training and validation datasets (Fig. 8, F to H, and fig. S17). Notably, Pearson's correlation coefficients between actual priming and predicted priming were greater for random forest models (Fig. 8H) relative to linear mathematical models (Fig. 8C), indicating that nonlinear mathematical models may be superior predictors of priming. Last, to evaluate the importance of each protein to the model, we evaluated the mean decrease accuracy for each protein (Fig. 8I). Bak was an important parameter in the random forest models for all tumors, while the anti-apoptotic protein Bcl-XL was the only important parameters in two of the five tumors (Fig. 8I).

DISCUSSION

A key advance presented in this study is the consecutive measurement of phenotype and molecular state on the same single cancer cell. This is performed in non-genetically modified cells and is applicable to primary mouse or human tissue. Many multiplexed or high-dimensional molecular measurements are not accompanied by direct measurement of phenotype and typically infer phenotype based on protein/transcript level and prior pathway knowledge (8). However, direct measurement of phenotypes enables the grounding of the molecular measurements to a phenotypic truth. This enables functional evaluation of molecularly defined subpopulations (Figs. 5 and 7), as well as the development and validation of single-cell models that describe how proteins contribute to apoptotic priming at the single-cell level (Fig. 8). A notable finding from these models of priming is that univariate single-cell correlates of molecules to phenotypes can be misleading. For example, in COCA61 while the pro-apoptotic protein Bak was a poor univariate correlate of priming, it contributed to the model of apoptotic
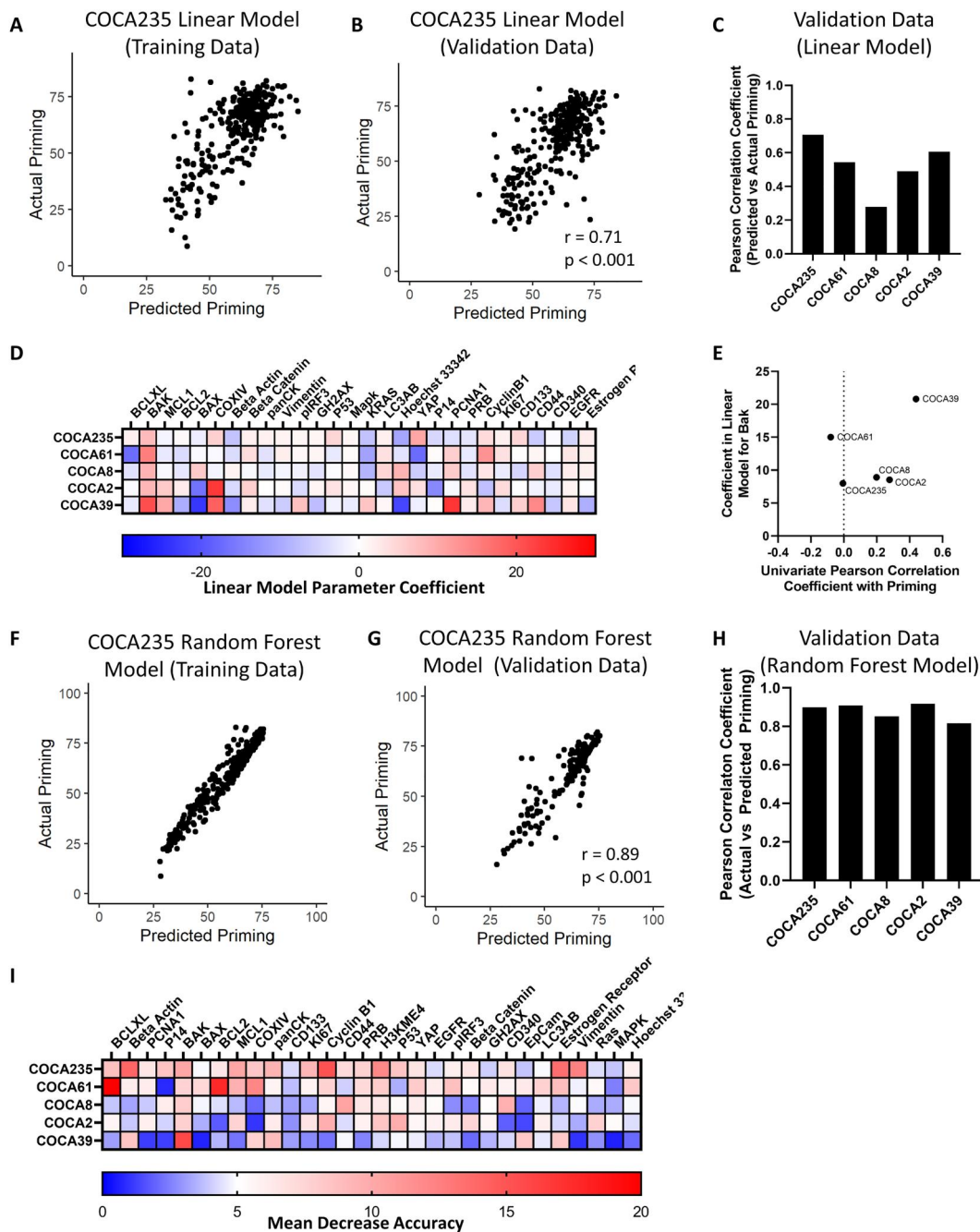
Fig. 8. Linear and random forest mathematical models of apoptotic priming in colon PDX tumors. (**A**) Comparison of actual and predicted priming for the training dataset for COCA235. (**B**) Comparison of actual and predicted priming for the validation dataset for COCA235. Pearson's correlation *r* was calculated between actual and predicted priming. (**C**) Pearson's correlation coefficients of actual and predicted priming for validation data for each tumor-specific model. (**D**) Coefficient for each protein parameter for each linear model of priming. (**E**) Comparison of the Pearson's correlation between Bak expression with priming (*x* axis), and the linear model coefficient for Bak. Each dot represents a single colon PDX model. (**F**) Comparison of actual and predicted priming for random forest models for COCA235 using a training dataset. (**G**) Comparison of actual and predicted priming for random forest models for COCA235 using the validation dataset. Pearson's correlation *r* was calculated between actual and predicted priming. (**H**) Pearson's correlation coefficient of actual and predicted priming for validation data for random forest models. (**I**) Evaluation of protein level value to random forest models using mean decrease accuracy. Data represent a merge of *N* = 2 biological replicates.

priming (Fig. 8, D and I). Ultimately, co-phenotypic and proteomic single-cell measurement of apoptosis phenotypes is enabled by an early, pre-protease, and pre-nuclease measurement of cell death. Other early measurements of cell death may be valuable including changes in cell mass and changes in cell morphology (*17*, *18*).

While the consecutive measurement of apoptotic priming by BH3 profiling and multiplexed immunofluorescence may identify features of poorly primed cells, we note that there are limitations to this strategy. First, while BH3 profiling evaluates whether cells are primed for mitochondrial-mediated apoptosis, it does not evaluate sensitivity to other forms of cell death such as ferroptosis (*19*). Second, if antibody recognition of proteins is poor, we may miss proteins that are positively or negatively correlated with apoptotic priming.

This study provides an additional functional demonstration that there is pretreatment variability of the baseline apoptotic sensitivity in primary mouse tumors. A common caveat when measuring any phenotypic variability is confounding assay noise. However, demonstrating that there are univariate correlates (Fig. 6) and multivariate nonlinear models that correspond to apoptotic priming (Fig. 8) suggests that pretreatment variability of apoptotic priming is rooted in molecular differences between cells and is not simply assay noise. In addition, the variability of apoptotic priming suggests not only that chemotherapy may have variable activity on cells but also that some cells require more therapy-induced pro-apoptotic signaling to undergo frank cell death.

Mathematical modeling of apoptotic sensitivity may have value as biomarkers or in drug development (*8*). However, while mathematical models could the predict priming of specific PDXs (Fig. 8, F to H), the parameters of the models were quite different (Fig. 8I) indicating that there was no single mathematical model that could predict apoptotic priming for all PDXs. One potential reason for the flawed modeling is missing proteins that are known to be involved in apoptosis, but for which immunofluorescence is poor. Moreover, proteins that we are measuring with immunofluorescence may have posttranslational modifications or subcellular localizations that alter apoptotic activity but may not be easily measured (*20*). We also anticipate that there are proteins of which we are unaware that are involved in apoptosis (*21*). Last, the variability of the mathematical models of apoptotic priming across different PDXs may simply indicate that there are various ways in which a tumor can acquire apoptotic resistance which may be practically difficult to model. Ultimately, though insights can be gained from the high-plex protein measurements, these are almost certainly incomplete, and measurements of phenotypes remain valuable.

A potential output for consecutive measurements of key cancer phenotypes and multiplexed protein measurements is the identification of targetable features of poorly primed cancer cells within a tumor. In four of six colon PDX models, we find that low expression of the Bak protein is associated with poor apoptotic priming (Fig. 6). Therapeutic strategies that globally increase Bak expression may eliminate a larger fraction of tumors. In addition, we identified instances where linear models suggested that druggable proteins correlate with poor apoptotic priming. For example, in COCA61, the Bcl-XL protein is correlated with poor apoptotic priming (Fig. 7) and can be targeted by navitoclax or by DT2216 (*22*, *23*). In addition, in COCA235, the Mcl-1 protein, which can be inhibited by AZD5991 (*24*), was correlated with poor apoptotic priming (Fig. 7). This suggests that, for these tumors, combinations of chemotherapies with these drugs may result in a more complete clinical response. Neither Bcl-XL nor Mcl-1 corresponds with poor apoptotic priming in all PDX models. This indicates that the maximal benefit of targeting poorly primed cells may require a personalized strategy.

MATERIALS AND METHODS
Cell culture
HeLa, MDA-MB-231, and MDA-MB-468 MCF7 cells were cultured in Dulbecco's modified Eagle's medium (DMEM)/F-12 (Life Technologies, 11995073), 10% fetal bovine serum (FBS) (Life Technologies, 10437028), and penicillin/streptomycin (Life Technologies, 15140122). Freshly isolated mice colon tumors were cultured in Advanced DMEM/F-12 (Life Technologies, 12491015), 10% FBS, penicillin/streptomycin, N2 (Life Technologies, 17502048), and B27 (Life Technologies, 17504044).

PDX tumor dissociation
For colon PDX tumors, tissue to establish PDX models was obtained according to Institutional Review Board–approved research protocols (14-030). Fresh primary colorectal cancer biopsies were first incubated in an antibiotic cocktail of penicillin/streptomycin/amphotericin B/ciprofloxacin for 1 to 2 hours and implanted into the flanks of 5-week-old, female nude mice (Nu/Nu; Taconic). Tumors were first cut into small pieces using a scalpel and mechanically dissociated using a Miltenyi gentleMACS Dissociator. Cells were incubated for 20 min in Advanced DMEM/F-12, 10% FBS, penicillin/streptomycin, N2, and B27, with dissociation enzymes collagenase IV (16,000 U/ml; Life Technologies, 17104019), and hyaluronidase (10,000 U/ml; Worthington, LS002594). Cells were filtered through a 500-μm cell strainer (Thermo Fisher Scientific, NC0822591), and cell viability was assessed by trypan blue.

Real-time BH3 profiling on cell lines
Cell lines were seeded at 25,000 cells per well in a 96-well collagen-coated plate and incubated overnight at 37°C. To begin the RTBP, cells were stained with Hoechst (5 μg/ml; Life Technologies, 62249). Cells were subsequently washed twice in Derived from Trehalose Experimental Buffer (DTEB) [135 mM trehalose, 10 mM Hepes, 50 mM KCl, 0.005 mM EGTA, 0.02 mM EDTA, 0.1% protease-free bovine serum albumin, and 5 mM succinate (pH 7.4)] with oligomycin (0.02 mg/ml; Sigma-Aldrich, O4876) and 0.025 μM TMRE (Life Technologies, T669). This buffer was removed and a DTEB buffer with 0.002% digitonin (Sigma-Aldrich, D5628) was added. The plate was then imaged, taking a picture of each well every 3 min for 11 cycles. Peptides were subsequently added to each well. Peptides used included BIM, BCL2 associated agonist of cell death (BAD), p53 upregulated modulator of apoptosis (PUMA), BID, Mcl-1 specific peptide 1 (MS1), and Bfl-1 specific peptide 1 (FS1) at concentrations ranging from 0.1 to 100 μM. The plate was then imaged again, taking a picture of each well every 3 min for 32 cycles. At the completion of the second round of imaging, the plate was removed and a concentration of 4% paraformaldehyde (PFA) was added to each well for 45 min, and then neutralized with an N2 buffer.

Real-time BH3 profiling on PDX models

PDX cells seeded at 15,000 cells per well in a 384-well collagen-coated plate. To begin the RTBP, plates were washed six times in a DTEB buffer with oligomycin (0.02 mg/ml) and 0.025 μM TMRE using the BioTek 406EL plate washer. A mixture of DTEB with oligomycin (0.02 mg/ml), 0.025 μM, and digitonin (0.025 μM) was added to each well. The plate was then imaged, taking a picture of each well every 3 min for 11 cycles. Subsequently, the synthetic BH3 peptide was added to each well. The plate was then imaged again, taking a picture of each well every 3 min for 32 cycles. At the completion of the second round of imaging, the plate was removed and a concentration of 4% PFA was added to each well for 45 min, and then neutralized with an N2 buffer.

Cycling immunofluorescence

Cycling immunofluorescence was performed as described in (7). Briefly, cells were stained with dye-conjugated antibodies with non-overlapping emission/excitation properties. A list of antibodies is provided in table S1. After overnight staining, cells were washed and imaged. To inactivate fluorescent dyes, the wells were bleached with 3% hydrogen peroxide (Sigma-Aldrich, 216763) and 20 mM sodium hydroxide (Sigma-Aldrich, S5881) in a base solution of phosphate-buffered saline. Plates were exposed to light for 1 hour. Plates were imaged after bleaching to confirm dye inactivation. In instances where dyes were not completely inactivated, another cycle of bleaching was performed. Plates were subsequently stained with additional antibodies. This process was repeated over several cycles.

Imaging and image analysis

All imaging was performed on the ImageXpress Micro XLS High-Content Widefield Microscope (Molecular Devices). A 10× widefield objective was used to perform all imaging. For live-cell imaging, rolling ball subtraction was performed in ImageJ. For time-lapse images, image registration (the alignment of images over time) was performed in ImageJ. Analysis of cell locations and intensities was performed in CellProfiler. Custom R scripts were used to track single cells on the basis of CellProfiler outputs. Automated analysis of priming including the calculation of area under TMRE versus time curves was calculated in R. Graphs were produced using the ggplot or Plotly libraries in R, or in GraphPad Prism. CyCIF was performed as described in (7). Images collected during CyCIF were collected with the same microscope and objective as the live-cell imaging. A rolling ball background subtraction and image registration of all CyCIF cycles were performed in ImageJ. Intensities of CyCIF images were calculated in CellProfiler. Custom R scripts were used to link the position of cells during live-cell imaging to the position of cells during the CyCIF cycles. All ImageJ macros, CellProfiler pipelines, and custom R scripts are available on request. Heatmaps and dot plots include merged data from all replicates.

Statistics

t tests and receiver operating characteristic analyses were performed in GraphPad Prism. Correlation analyses were performed in R or in GraphPad Prism.

Mathematical modeling of priming

All mathematical modeling of priming based on protein measurements was carried out in R. For linear models, we split the dataset in half for a training and validation dataset. Multiple linear regression was performed using the lm() function. Visual and statistical evaluations of the linear model on the validation dataset were performed in R. Random forest modeling of priming based on protein measurements was performed in R using the randomForest library. The data were split into a training dataset (70% of all cells) and a validation dataset (30% of cells). A default of 500 trees was used.

Supplementary Materials

This PDF file includes:
Figs. S1 to S17
Table S1
Legends for movies S1 to S5

Other Supplementary Material for this manuscript includes the following:
Movies S1 to S5

View/request a protocol for this paper from *Bio-protocol*.

REFERENCES AND NOTES

1. M. M. Dix, G. M. Simon, B. F. Cravatt, Global mapping of the topography and magnitude of proteolytic events in apoptosis. *Cell* **134**, 679–691 (2008).

2. X. Liu, H. Zou, C. Slaughter, X. Wang, DFF, a heterodimeric protein that functions downstream of caspase-3 to trigger DNA fragmentation during apoptosis. *Cell* **89**, 175–184 (1997).

3. M. Certo, V. D. G. Moore, M. Nishino, G. Wei, S. Korsmeyer, S. A. Armstrong, A. Letai, Mitochondria primed by death signals determine cellular addiction to antiapoptotic BCL-2 family members. *Cancer Cell* **9**, 351–365 (2006).

4. T. Ni Chonghaile, K. A. Sarosiek, T.-T. Vo, J. A. Ryan, A. Tammareddi, V. D. G. Moore, J. Deng, K. C. Anderson, P. Richardson, Y.-T. Tai, C. S. Mitsiades, U. A. Matulonis, R. Drapkin, R. Stone, D. J. Deangelo, D. J. Mc Conkey, S. E. Sallan, L. Silverman, M. S. Hirsch, D. R. Carrasco, A. Letai, Pretreatment mitochondrial priming correlates with clinical response to cytotoxic chemotherapy. *Science* **334**, 1129–1133 (2011).

5. T.-T. Vo, J. Ryan, R. Carrasco, D. Neuberg, D. J. Rossi, R. M. Stone, D. J. DeAngelo, M. G. Frattini, A. Letai, Relative mitochondrial priming of myeloblasts and normal HSCs determines chemotherapeutic success in AML. *Cell* **151**, 344–355 (2012).

6. S. C. Bendall, E. F. Simonds, P. Qiu, E. A. D. Amir, P. O. Krutzik, R. Finck, R. V. Bruggner, R. Melamed, A. Trejo, O. I. Ornatsky, R. S. Balderas, S. K. Plevritis, K. Sachs, D. Pe'er, S. D. Tanner, G. P. Nolan, Single-cell mass cytometry of differential immune and drug responses across a human hematopoietic continuum. *Science* **332**, 687–696 (2011).

7. J.-R. Lin, M. Fallahi-Sichani, P. K. Sorger, Highly multiplexed imaging of single cells using a high-throughput cyclic immunofluorescence method. *Nat. Commun.* **6**, 8390 (2015).

8. A. U. Lindner, M. Salvucci, E. McDonough, S. Cho, X. Stachtea, E. P. O'Connell, A. D. Corwin, A. Santamaria-Pang, S. Carberry, M. Fichtner, S. van Schaeybroeck, P. Laurent-Puig, J. P. Burke, D. A. McNamara, M. Lawler, A. Sood, J. F. Graf, M. Rehm, P. D. Dunne, D. B. Longley, F. Ginty, J. H. M. Prehn, An atlas of inter- and intra-tumor heterogeneity of apoptosis competency in colorectal cancer tissue at single-cell resolution. *Cell Death Differ.* **29**, 806–817 (2022).

9. J.-R. Lin, B. Izar, S. Wang, C. Yapp, S. Mei, P. M. Shah, S. Santagata, P. K. Sorger, Highly multiplexed immunofluorescence imaging of human tissues and tumors using t-CyCIF and conventional optical microscopes. *eLife* **7**, e31657 (2018).

10. P. D. Bhola, E. Ahmed, J. L. Guerriero, E. Sicinska, E. Su, E. Lavrova, J. Ni, O. Chipashvili, T. Hagan, M. S. Pioso, K. McQueeney, K. Ng, A. J. Aguirre, J. M. Cleary, D. Cocozziello, A. Sotayo, J. Ryan, J. J. Zhao, A. Letai, High-throughput dynamic BH3 profiling may quickly and accurately predict effective therapies in solid tumors. *Sci. Signal.* **13**, eaay1451 (2020).

11. P. D. Bhola, B. G. Mar, R. C. Lindsley, J. A. Ryan, L. J. Hogdal, T. T. Vo, D. J. DeAngelo, I. Galinsky, B. L. Ebert, A. Letai, Functionally identifiable apoptosis-insensitive subpopulations determine chemoresistance in acute myeloid leukemia. *J. Clin. Invest.* **126**, 3827–3836 (2016).

12. D. S. Potter, R. Du, P. Bhola, R. Bueno, A. Letai, Dynamic BH3 profiling identifies active BH3 mimetic combinations in non–small cell lung cancer. *Cell Death Dis.* **12**, 741 (2021).

13. P. D. Bhola, A. L. Mattheyses, S. M. Simon, Spatial and temporal dynamics of mitochondrial membrane permeability waves during apoptosis. *Biophys. J.* **97**, 2222–2231 (2009).

14. A. Letai, M. C. Bassik, L. D. Walensky, M. D. Sorcinelli, S. Weiler, S. J. Korsmeyer, Distinct BH3 domains either sensitize or activate mitochondrial apoptosis, serving as prototype cancer therapeutics. *Cancer Cell* **2**, 183–192 (2002).

15. C. Fraser, J. Ryan, K. Sarosiek, BH3 profiling: A functional assay to measure apoptotic priming and dependencies. *Methods Mol. Biol.* **1877**, 61–76 (2019).

16. F. Schönenberger, A. Deutzmann, E. Ferrando-May, D. Merhof, Discrimination of cell cycle phases in PCNA-immunolabeled cells. *BMC Bioinformatics* **16**, 180 (2015).

17. J. C. Caicedo, S. Singh, A. E. Carpenter, Applications in image-based profiling of perturbations. *Curr. Opin. Biotechnol.* **39**, 134–142 (2016).

18. M. A. Stockslager, S. Malinowski, M. Touat, J. C. Yoon, J. Geduldig, M. Mirza, A. S. Kim, P. Y. Wen, K.-H. Chow, K. L. Ligon, S. R. Manalis, Functional drug susceptibility testing using single-cell mass predicts treatment outcome in patient-derived cancer neurosphere models. *Cell Rep.* **37**, 109788 (2021).

19. V. S. Viswanathan, M. J. Ryan, H. D. Dhruv, S. Gill, O. M. Eichhoff, B. Seashore-Ludlow, S. D. Kaffenberger, J. K. Eaton, K. Shimada, A. J. Aguirre, S. R. Viswanathan, S. Chattopadhyay, P. Tamayo, W. S. Yang, M. G. Rees, S. Chen, Z. V. Boskovic, S. Javaid, C. Huang, X. Wu, Y. Y. Tseng, E. M. Roider, D. Gao, J. M. Cleary, B. M. Wolpin, J. P. Mesirov, D. A. Haber, J. A. Engelman, J. S. Boehm, J. D. Kotz, C. S. Hon, Y. Chen, W. C. Hahn, M. P. Levesque, J. G. Doench, M. E. Berens, A. F. Shamji, P. A. Clemons, B. R. Stockwell, S. L. Schreiber, Dependency of a therapy-resistant state of cancer cells on a lipid peroxidase pathway. *Nature* **547**, 453–457 (2017).

20. J. Kale, O. Kutuk, G. C. Brito, T. S. Andrews, B. Leber, A. Letai, D. W. Andrews, Phosphorylation switches Bax from promoting to inhibiting apoptosis thereby increasing drug resistance. *EMBO Rep.* **19**, e45235 (2018).

21. P. D. Bhola, A. Letai, Mitochondria-judges and executioners of cell death sentences. *Mol. Cell* **61**, 695–704 (2016).

22. S. Khan, X. Zhang, D. Lv, Q. Zhang, Y. He, P. Zhang, X. Liu, D. Thummuri, Y. Yuan, J. S. Wiegand, J. Pei, W. Zhang, A. Sharma, C. R. McCurdy, V. M. Kuruvilla, N. Baran, A. A. Ferrando, Y. M. Kim, A. Rogojina, P. J. Houghton, G. Huang, R. Hromas, M. Konopleva, G. Zheng, D. Zhou, A selective BCL-X$_L$ PROTAC degrader achieves safe and potent antitumor activity. *Nat. Med.* **25**, 1938–1947 (2019).

23. C. Tse, A. R. Shoemaker, J. Adickes, M. G. Anderson, J. Chen, S. Jin, E. F. Johnson, K. C. Marsh, M. J. Mitten, P. Nimmer, L. Roberts, S. K. Tahir, Y. Xiao, X. Yang, H. Zhang, S. Fesik, S. H. Rosenberg, S. W. Elmore, ABT-263: A potent and orally bioavailable Bcl-2 family inhibitor. *Cancer Res.* **68**, 3421–3428 (2008).

24. A. E. Tron, M. A. Belmonte, A. Adam, B. M. Aquila, L. H. Boise, E. Chiarparin, J. Cidado, K. J. Embrey, E. Gangl, F. D. Gibbons, G. P. Gregory, D. Hargreaves, J. A. Hendricks, J. W. Johannes, R. W. Johnstone, S. L. Kazmirski, J. G. Kettle, M. L. Lamb, S. M. Matulis, A. K. Nooka, M. J. Packer, B. Peng, P. B. Rawlins, D. W. Robbins, A. G. Schuller, N. Su, W. Yang, Q. Ye, X. Zheng, J. P. Secrist, E. A. Clark, D. M. Wilson, S. E. Fawell, A. W. Hird, Discovery of Mcl-1-specific inhibitor AZD5991 and preclinical activity in multiple myeloma and acute myeloid leukemia. *Nat. Commun.* **9**, 5341 (2018).

Science Advances

Sequential apoptotic and multiplexed proteomic evaluation of single cancer cells

Emmalyn Lecky, Atreyi Mukherji, Rebecca German, Gabriella Antonellis, Jia-Ren Lin, Michael Yorsz, Kelley E. McQueeney, Jeremy Ryan, Kimmie Ng, Ewa Sicinska, Peter K. Sorger, Anthony Letai, and Patrick D. Bhola

View the article online
https://www.science.org/doi/10.1126/sciadv.adg4128
Permissions
https://www.science.org/help/reprints-and-permissions

Use of this article is subject to the Terms of service